Closed-loop position control of a self-sensing 3-DoF origami module with pneumatic actuators

Mustafa Mete and Jamie Paik*

***Abstract*— This paper presents closed-loop position control of a pneumatically actuated modular robotic platform "pneumagami" that can be stacked to enlarge work and design space for wearable applications. The module is a 3 degrees of freedom (DoF) parallel robot with two rotational and one translational motion, which is actuated by three antagonistic pneumatic pouch motor pairs attached to three leg joints. To control the pouch motors, we utilize miniature proportional valves. As for the sensing, we introduce a novel embedded resistive sensor mechanism utilizing rotary-to-translational transmission. The sensor's transmission is modeled and verified by experiments. Furthermore, we study analytic forward and inverse kinematic models of the pneumagami module. Utilizing the models, we design a closed-loop feedback controller to track two different trajectories. The experimental results show that the module follows the desired trajectories successfully. Thus, we report that the proposed pneumagami modules can be utilized for achieving a controllable robotic third arm with higher DoFs and range of motion (RoM) when connected in series.**

***Index Terms*— origami robots, wearable robots, pneumatic actuators, embedded sensor, parallel kinematics, closed-loop control, position control, trajectory tracking**

I. INTRODUCTION

Robotic limbs providing task assistance and support constitute one of the developing areas in wearable robotics. Many researchers have proposed different robotic limbs designs and methods. In [1]–[4], wearable robotic third and fourth arms assisting users with different tasks have been introduced. In [5] and [6], a supernumerary robotic forearm attached at the elbow has been proposed. Finally, in [7], a multipurpose serpentine robot with 25 DoF has been implemented. These robots are mode of rigid components that brings along the challenges with safe human-robot interaction (HRI).

To achieve safe human-robotic limb interaction, researchers have investigated soft robotic alternatives [8]–[12]. In terms of their form, these soft extra limbs can be classified as single-segmented [13]–[18] and multi-segmented [9], [10], [19]–[21]. However, in general, soft robots exhibit undesired deformations and twisting motions under external forces and have modeling and control challenges.

As an alternative to completely soft and completely rigid robotic limbs, researchers introduced origami-based mechanical continuum structures by leveraging origami design and fabrication techniques that enable the design of lightweight, scalable, and reconfigurable structures and robots. [22]–[30]. Those continuum structures and robots show both soft and rigid features by incorporating compliant hinges and rigid elements, enabling safe human-robot interaction and high load-carrying capacity. Furthermore, they provides high passive twisting stiffness, resolving the non-controllable twisting problem in soft continuum arms. In [31], a foldable lightweight, scalable, and stiff drone arm composed of Sarrus linkage modules has been proposed. The arm has only one DoF and one way actuation. The deployment of the arm count on the gravity and its own weight. In [32], a tendon-driven continuum robot composed of origami-inspired compliant modules with helical compression springs has been presented. The modules are connected to one tendon system, limiting the workspace of the arm due to the modules' coupled motion. In [33], [34], the workspace limitation from the previous work has been addressed by driving each module with a separate tendon system enabling uncoupled motion of the modules. However, in almost all of the tendon-driven origami-based continuum limbs, the proposed limbs can only be actuated in one-way. In other words, they count on the compression springs or torsional/axial stiffness of the origami structure for restoring the initial state or act against the external forces.

As alternatives to the tendon-driven actuators, various actuation methods integrated with origami designs have been investigated such as electronic motors [35], piezoelectric materials [36], shape memory alloys (SMAs) and polymers (SMPs) [37], magnetics [38], and dielectric elastomers [39]. Apart from these methods, pneumatic actuation method offers some advantages over the previous methods, such as a high power-to-weight ratio, intrinsic compliance, safe actuation, and relatively fast actuation [40]–[42]. Especially, planar pneumatic pouch actuators provide easy integration with origami-inspired mechanisms. However, precise control of the pouch motors is still a challenge [43]–[45].

When it comes to the closed-loop control of the origami extra robotic limbs, motion capture systems provide fast and accurate position feedback. However, they are limited to highly controllable research or laboratory environment. Angle sensing for origami folds is an option to calculate the robot position when combined with kinematic relations. Different sensors have been explored for sensing the fold angles such as strain gauges [46], Hall-effect sensors [38], liquid metal sensors [45], piezoresistive angle sensors [47], and phototransistor and infrared light-emitting diode (LED) pairs [48]. However, existing sensing methods suffer from drift over time, distortions due to external factors such as temperature, magnetic field, and light.

Recently, an origami-inspired modular robotic pneumagami platform actuated by pouch motors has been proposed [49] by leveraging the advantages of modular soft and origami robots

This work was supported the Swiss National Science Foundation (SNSF) and the National Centre of Competence in Research (NCCR) Robotics (Switzerland).

Mustafa Mete and Jamie Paik are with the Reconfigurable Robotics Laboratory, EPFL, 1015 Lausanne, Switzerland
*For correspondance email: jamie.paik@epfl.ch

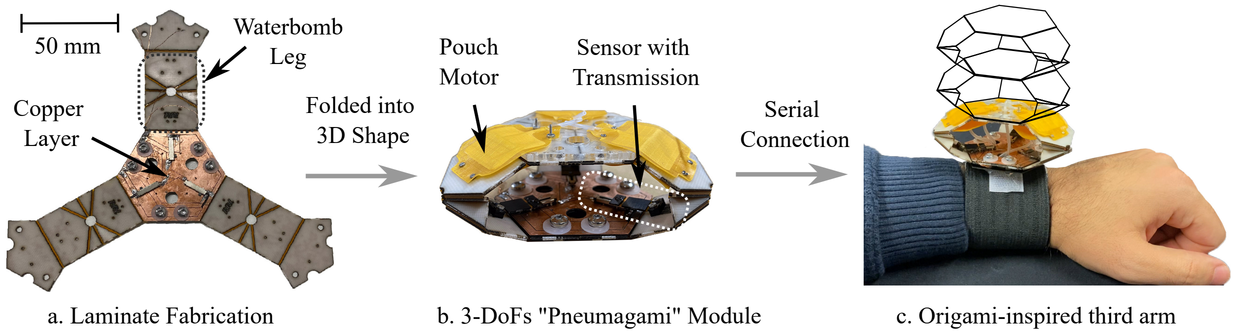

Fig. 1. **Soft actuator-based parallel origami module design and construction:** by utilizing laminate fabrication, we stack FR4, adhesive, and Kapton layers with specific shape and folding patterns and form the module frame. Then, we place copper and resistive layer utilized for embedded angle sensing (a). Finally, we attach planar pouch pairs and fold the flat structure into a 3D shape. We obtain a 3 DoFs module with a closed kinematic chain (b). This compliant and lightweight module with pneumatic actuation and embedded sensing can be connected in series to construct a supernumerary origami-inspired robotic continuum arm (c).

[21], [35]. The design enables reconfigurable and high DoF systems with built-in compliance. The module performance and properties have been characterized, and an open-loop on/off control has been applied. Here, we present a follow-up study that focuses on high fidelity closed-loop position control of a pneumatically actuated origami-inspired module with novel embedded sensors to be potentially used for lightweight, reconfigurable, and safe extra robotic limbs as shown in Figure 1.

In this paper, first, we study the forward and inverse kinematics of the 3-DoFs origami-inspired parallel module inspired by Canfield mechanism [50]–[52], in which three independent waterbomb legs dictate the workspace of the module. Second, we propose a novel sensing method utilizing an embedded resistive layer with translational-to-rotary transmission to reliably measure the folding angle for estimating the module end effector's positions and orientation. Utilizing the proposed sensing method, we can easily distribute the sensors to many folding joints. Third, we apply closed-loop position control and trajectory tracking driven by soft pneumatic pouch actuators utilizing proposed forward and inverse kinematic models for the sensor transmission and the module.

The main contributions can be summarized as:

- A novel embedded angle sensing method with translational-to-rotary transmission, which is easily distributable to many origami folds
- Forward and inverse kinematic analysis of the module and sensor transmission and experimental validation of the models
- High fidelity closed-loop control of parallel origami structures with embedded sensors, driven by soft pneumatic pouch motors

II. Module Design

A 3-DoF pneumagami module [49] incorporates compliant folding hinges and rigid laminates with specific folding patterns. Its frame is composed of three parts: a base hexagon, a top hexagon, and three identical waterbomb legs serving as spherical joints. We utilize layer-by-layer manufacturing method for the fabrication of the frame. Then, we attach three antagonistic planar pouch motor pairs to three leg joints for two-way joint actuation. Then, we fold the structure into a 3D parallel mechanism. The mechanism design provides 3 DoF motion (two rotational and one translational), fully controllable with three leg joints. When collapsed, the module goes to a quasi-flat shape. The proposed design allows the construction of a continuum robotic arm by a serial connection of the modules as shown in Figure 1.

Unlike [49], this new design incorporates embedded sensors and proportional valves to enable high fidelity closed-loop position control of the module. We have copper and resistive layers attached to the base for achieving embedded folding angle sensors in this new design. The novel sensor, explained in more detail in the next section, enables feedback control of the module. Moreover, instead of solenoid valves, we utilize proportional valves. While solenoid valves have an on/off working principle, proportional valves can control the airflow proportionally with applied current or voltage. Thus, they enable more precise modulation of the output pressure.

The mini proportional valves used in the control setup have only two ports which means they do not have exhaust. When the valve is closed, the air in the pouch cannot be released. Therefore, the pouch motor always stays inflated. The first solution is to use two valves for each pouch motor and control the input and exhaust airflow. The second solution is to open a circular hole with 0.5 *mm* radius on the pouch to have a constant exhaust to reduce the number of valves required. Thus, we only control the input airflow. Although the hole size affects the max pressure, bandwidth, and control performance, we chose the second option in order to reduce the cost.

III. Novel Sensing Mechanism

Sensing of fold angles allows obtaining the position and orientation of pneumagami's end effector when combined with reliable kinematic models. Here, we introduce a novel, precise *embeddable angle sensor and its mechanism*. To measure the folding angle, we place a copper and resistive layer on the base hexagon and a sliding laminate linkage, slider, on the resistive layer. The traces on the copper layer allows the current to pass through the resistive layer. We constrain the slider's motion to one DoF translational motion.

The slider is connected to the rotating arm by a connecting linkage equivalent to a compliant slider-crank mechanism or origami slider joint [38] as illustrated in Figure 2. When the arm is rotated, the slider moves on the resistive layer and changes the measured resistance like a linear potentiometer. From the resistance change, we find the linear displacement. Finally, from the displacement, we calculate the folding angle utilizing transmission kinematics.

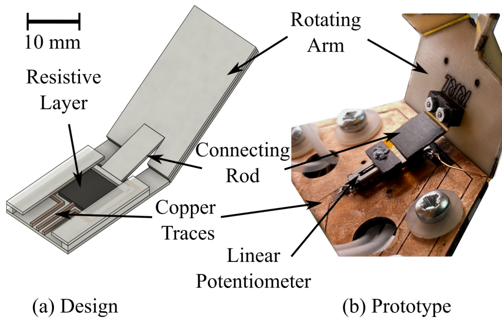

Fig. 2. **Embedded sensor mechanism and design:** We place an origami slider connected to the rotating arm on copper and resistive layers. When the arm rotates, the slider mechanism converts rotational motion into one DoF translational motion. The slider moves on the resistive layer and changes the measured resistance. By utilizing the kinematics of the transmission, we measure the folding angle.

Instead of creating a custom resistive layer and characterizing and optimizing its performance, we utilize off-the-shelf mini linear potentiometers as resistive layers for simplicity. We connect the slider to the potentiometer shaft by cutting a hole on the slider with a high-accuracy laser-cutter. We manually assemble the slider and the potentiometer as demonstrated in Figure 2. Although mini potentiometers provide reliable output performance in terms of linearity, operating life, and tolerance, embedding resistive layers by using inkjet printing or adding graphite or carbon films will allow the design of highly customizable and scalable sensors. Also, it will enable easy integration of the sensor with the laminate fabrication method and, therefore, require no manual assembly. In future work, we plan to try previously described techniques and investigate sensor performance.

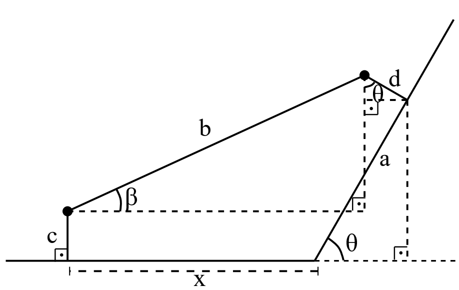

Fig. 3. Sensor kinematic model in 2D

To convert voltage reading to the folding angle and vice versa, we study the forward and inverse kinematics of the transmission. We analyze the transmission in 2D as shown in Figure 3. a,b,c,d, and x represent the distance between the axis of rotation and the rod's connection point to the arm, the length of connecting rod, first offset, second offset, and the horizontal distance of the slider center to the axis of rotation respectively. θ, and β stands for the folding angle of leg and the angle between connecting rod and resistive layer, respectively. We write the kinematic relation as follows:

$$x = b \cdot cos(\beta) - a \cdot cos(\theta) + d \cdot sin(\theta) \tag{1}$$

$$\beta = \arcsin\left(\frac{a \cdot sin(\theta) + d \cdot cos(\theta) - c}{b}\right) \tag{2}$$

If we substitute (2) into (1), we obtain

$$x^2 + \sigma_1 \cdot x + \sigma_2 = 0 \tag{3}$$

where

$$\sigma_1 = 2a \cdot cos(\theta) - 2d \cdot sin(\theta)$$
$$\sigma_2 = a^2 - b^2 + c^2 + d^2 - 2c(d \cdot cos(\theta) + a \cdot sin(\theta))$$

When we solve the second-order polynomial equation, we obtain

$$x_{1,2} = \frac{-\sigma_1 \pm \sqrt{\sigma_1^2 - 4\sigma_2}}{2},\ x > 0 \tag{4}$$

Thus, we calculate the linear from the folding angle θ by the previous forward kinematic equations. However, to calculate the folding angle from the linear displacement reading, we need the inverse kinematic model. In other words, we need to derive the θ as a function of x. Therefore, we modify the equation (3) by applying tangent half-angle substitution and obtain a second-order polynomial equation.

$$cos(\theta) = \frac{1-t^2}{1+t^2},\ sin(\theta) = \frac{2t}{1+t^2},\ t = \tan\frac{\theta}{2} \tag{5}$$

Substituting (5) into (3) gives

$$\varepsilon_1 \cdot t^2 + \varepsilon_2 \cdot t + \varepsilon_3 = 0 \tag{6}$$

Solutions of the second-order polynomial equation

$$t_{1,2} = \frac{-\varepsilon_2 \pm \sqrt{\varepsilon_2^2 - 4\varepsilon_1\varepsilon_3}}{2\varepsilon_1} \tag{7}$$
$$\theta_{1,2} = 2\arctan(t_{1,2}),\ \theta \in [0, \pi]$$

Hence, this inverse kinematic equation allows us to convert the linear sensory reading to the actual folding angle.

To validate the proposed sensor kinematics model, we conduct an experiment as shown in Figure 4 and provide parameter values for sensor mechanism in Table I. Here, we keep the end effector parallel to the module base, change the height from 11 to 41 mm with 5 mm steps, and repeat the experiment four times. Then, we compare the model to the measured leg angles read by the embedded sensors in Figure 5. The measured data have 0.08 mm root mean square (RMS) displacement error. Moreover, the RMS error between the model and measured data is 2.2°. The errors can be attributed to measurement errors and small misalignment due to the manual assembly of potentiometers and connecting rods.

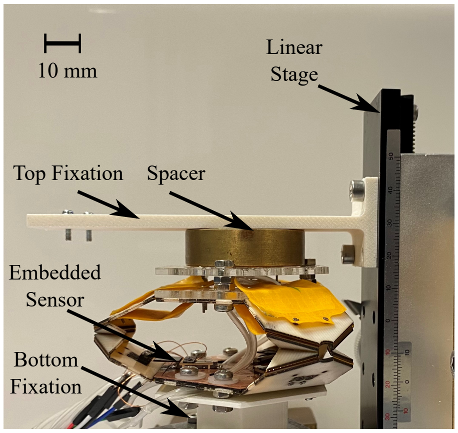

Fig. 4. **Sensor characterization:** We attach the module end effector to a linear stage using a spacer and a fixation. While keeping the module's top and bottom hexagons parallel, we increase the module's height by 5 *mm* steps by changing the position of the end effector manually. Then, we record the actual height and sensory data. Finally, using sensor kinematics, we calculate the leg angle.

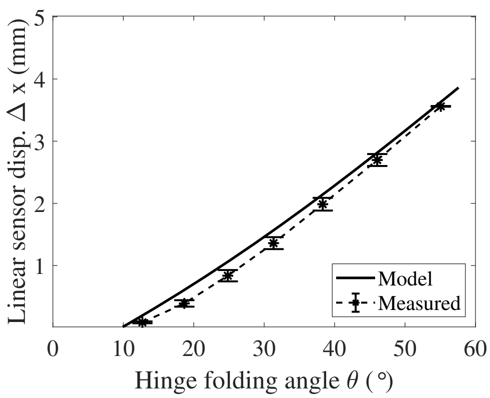

Fig. 5. **Model vs measured folding angle:** We repeat the experiment four times and plot the average measured data with error bars. Then, We compare it with the model. The RMS error between the model and measured data is around 2.2°.

IV. Kinematic Model Of The Module

We need inverse and forward kinematic models of the module to control the position of the module and calculate the end-effector position from angle sensory reading. The kinematics of the 3-DoF Canfield parallel mechanism has been analyzed in previous works [32], [50], [51]. We modify the inverse kinematic model to our hexagon base shape. When it comes to the forward kinematics, in [32], [51], since modules are driven by linear SMA and tendon actuators, researchers calculate the position and orientation of the end effector as functions of the input length variables, which are the distances between three top and bottom platform vertices. However, in our case, we drive a similar parallel mechanism with rotary inputs. Therefore, we obtain a forward kinematic model that gives the end effector's position and orientation as a function of leg angles.

A. Inverse Kinematics

To drive the pneumagami module to a specific configuration, we study the parallel mechanism's inverse kinematic model. The model provides the input leg angles φ_i corresponding to the position and orientation of the end effector center O_p with respect to the module base center O_b presented by (r_0, ψ, δ) in polar coordinates as illustrated in Figure 6.

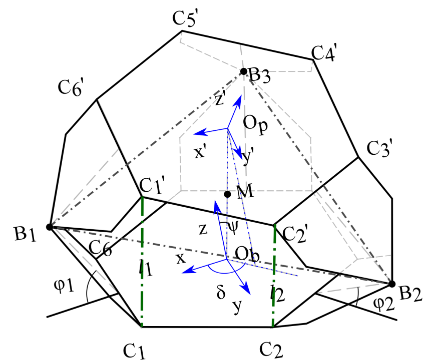

Fig. 6. Kinematic model of parallel pneumagami module and model parameters

B_i, C_i, and C_i' are the center of waterbomb legs, the corners of the base hexagon, and the corners of the top hexagon, respectively as seen in Figure 6. The top and bottom hexagons are symmetric with respect to the virtual plane passing through three waterbomb centers. XYZ and $X'Y'Z'$ are the local coordinate frames at the centers of the base O_b and top hexagon O_p, respectively. Let $\boldsymbol{r}_p$ represent the position vector from O_b to O_p given by

$$\boldsymbol{r}_p = r_0 \begin{bmatrix} \sin\psi\cos\delta \\ \sin\psi\sin\delta \\ \cos\psi \end{bmatrix} = r_0\,\boldsymbol{n} \tag{8}$$

where r_0 is the distance between O_b and O_p, $\boldsymbol{n}$ is the unit vector in the direction of $\boldsymbol{r}_p$, δ is the angle from X-axis to the projection of vector $\boldsymbol{r}_p$ to base hexagon plane, and, finally, ψ is the angle from Z-axis to $\boldsymbol{r}_p$.

The position vector $\boldsymbol{r}_p$ is perpendicular to the virtual plane due to the symmetry between the base and top hexagons with respect to the virtual plane. Let M be the intersection point of $\boldsymbol{r}_p$ and virtual plane, which is the midpoint of $\boldsymbol{O}_b\boldsymbol{O}_p$. Let $\boldsymbol{r}_{nm}$ represent the vector from M to N, which is an arbitrary point on the virtual plane.

$$\boldsymbol{r}_{nm} = \boldsymbol{r}_m - \boldsymbol{r}_n = \frac{r_0}{2}\begin{bmatrix} \sin\psi\cos\delta \\ \sin\psi\sin\delta \\ \cos\psi \end{bmatrix} - \begin{bmatrix} x \\ y \\ z \end{bmatrix} \tag{9}$$

Then, the following equation holds since $\boldsymbol{r}_m$ and $\boldsymbol{r}_{nm}$ are perpendicular to each other.

$$\boldsymbol{n}\cdot\boldsymbol{r}_{nm} = \boldsymbol{n}\cdot\boldsymbol{r}_n - \frac{r_0}{2} = 0 \tag{10}$$

The position of waterbomb centers B_i's with respect to XYZ coordinate frame is

$$\boldsymbol{b}_i = \begin{bmatrix} \cos\phi_i(r + l\cos\varphi_i) \\ \sin\phi_i(r + l\cos\varphi_i) \\ l\sin\varphi_i \end{bmatrix} \tag{11}$$

where $\phi_1 = 0$, $\phi_2 = 2\pi/3$, and $\phi_3 = 4\pi/3$. r and l represent the radius of the hexagon's inscribed circle and the half of arm length or, in other words, the distance from waterbomb center to the folding hinge.

Since the waterbomb centers B_i are on the virtual plane, they also satisfy the equation (10). Finally, we obtain the following equations by substituting (11) into (10).

$$l\cos\psi\sin\varphi_i + \sin\psi\cos(\delta - \phi_i)(r + l\cos\varphi_i) - \frac{r_0}{2} = 0 \tag{12}$$

In order to represent (12) in polynomial form, we apply tangent half-angle substitution as follows:

$$\cos\varphi_i = \frac{1 - {t_i}^2}{1 + {t_i}^2},\ \sin\varphi_i = \frac{2t_i}{1 + {t_i}^2},\ t_i = \tan\frac{\varphi_i}{2} \tag{13}$$

Finally, we derive the following second-order polynomial equation

$$a_i {t_i}^2 + d_i t_i + e_i = 0 \tag{14}$$

The solutions of equation (14) are

$$t_i = \frac{-d_i \pm \sqrt{{d_i}^2 - 4a_i e_i}}{2a_i}. \tag{15}$$

Finally, we calculate the input angles φ_i

$$\varphi_i = 2\arctan t_i,\ \varphi \in [0, /pi/2] \tag{16}$$

Thus, inverse kinematic equations (15) and (16) allow us to calculate the corresponding folding angles to a specific end-effector position and orientation.

B. Forward Kinematics

To calculate the end-effector position and orientation from the folding leg angles, we analyze the forward kinematics of the module. Since three waterbomb centers B_i are on the virtual plane, we can calculate the orthogonal vector N to the virtual plane as follows:

$$\boldsymbol{N} = (\boldsymbol{b}_1 - \boldsymbol{b}_2) \times (\boldsymbol{b}_1 - \boldsymbol{b}_3) \tag{17}$$

The distance from O_b the virtual plane is

$$d = \frac{(\boldsymbol{b}_1 - \boldsymbol{O}_b)\cdot\boldsymbol{N}}{|\boldsymbol{N}|} \tag{18}$$

The vector from the base to top hexagon centers $\boldsymbol{O}_b\boldsymbol{O}_p$ is parallel to the orthogonal vector N and its magnitude is equal to d. Thus, we can calculate the end effector's position $\boldsymbol{O}_p$ as follows:

$$\boldsymbol{O}_p = 2d\frac{\boldsymbol{N}}{|\boldsymbol{N}|} + \boldsymbol{O}_b \tag{19}$$

Using the forward kinematics equations, we derive reachable and actuated workspace of the module as shown in Figure 7. In the simulation, we use the module prototype dimensions given in Table I. The reachable workspace illustrates the maximum workspace that the module structure allows, while the actuated workspace shows the achievable workspace with pouch motors. There is difference between the two workspaces because pouch motors can achieve maximum 60°s folding angle whereas the structure allows 90°s folding angle. Therefore, we sweep the folding angles ϕ_i, $i \in [1,3]$ from 0 to $\pi/2$ and 0 to $\pi/3$ for reachable and actuated workspaces respectively. Finally, we scatter the end effector positions in the plot.

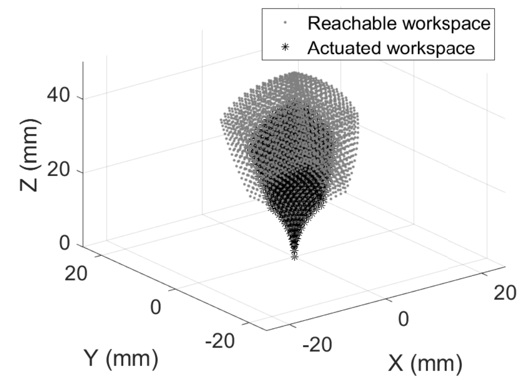

Fig. 7. **Current pneumagami module prototype workspace using forward kinematic model**: The plot shows the reachable workspace of the module without any actuator and achievable workspace with pouch motors. The workspace with actuator is limited since we can achieve 0 to 60°s folding at the legs with the pouch motors, whereas the structure design allows 0-90°s folding angle.

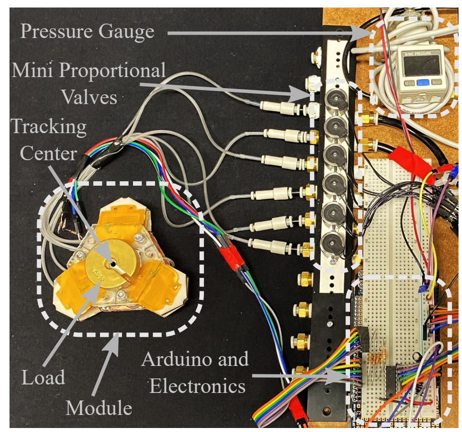

Fig. 8. **Experimental setup for pneumatic control:** the setup consists of six miniature proportional valves, a pressure gauge, an Arduino board, electronic components, flexible tubes, a load, and the module.

V. Closed-Loop Position Control

In this section, we apply closed-loop position control to the pneumagami module to track straight and circular trajectories. For the experiments, we create a prototype of the origami-inspired module whose design parameters and characteristics are given in Table I. There are six miniature proportional valves (VSO® LowPro) to drive six pouch motors embedded in the module surface.

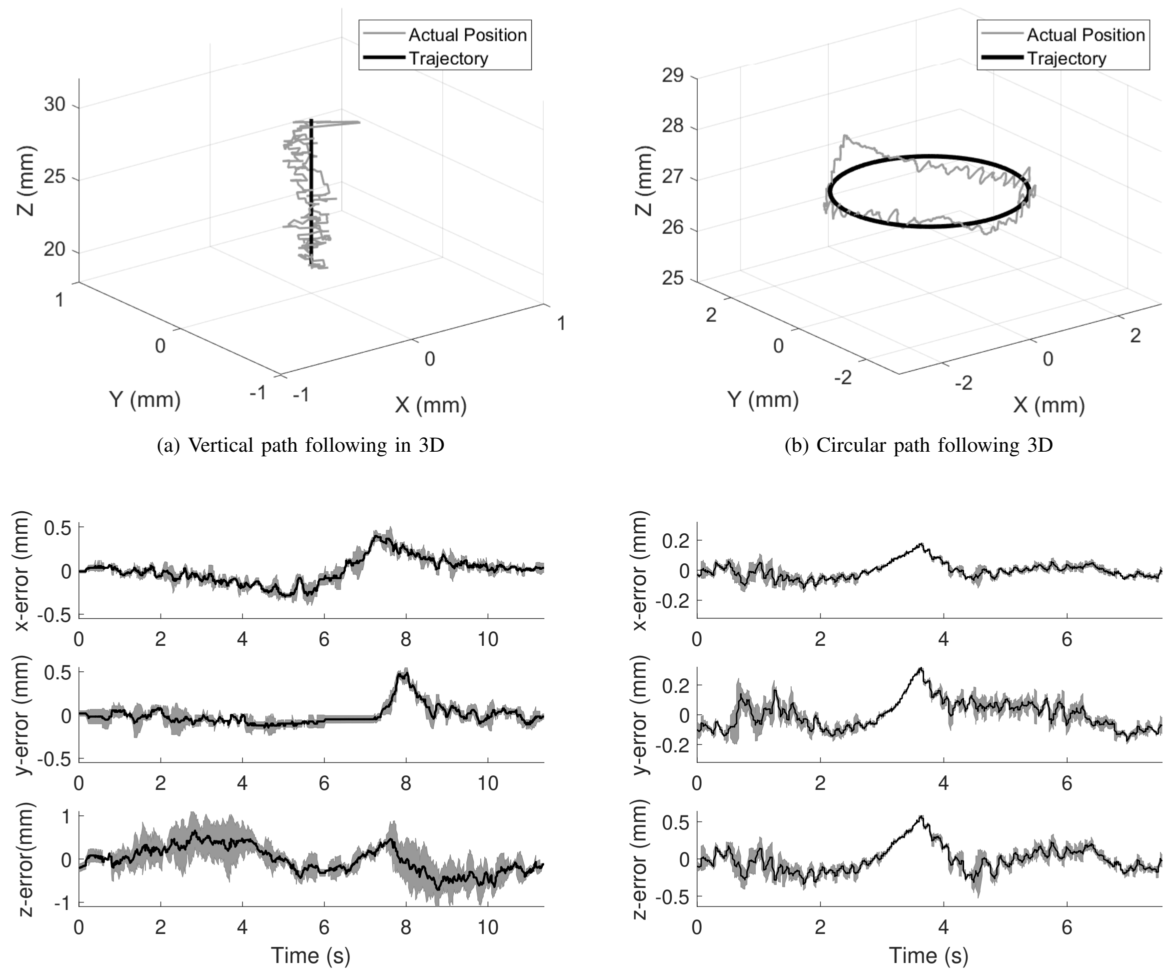

(a) Vertical path following in 3D

(b) Circular path following 3D

(c) Vertical path following RMS errors

(d) Circular path following RMS errors

Fig. 9. **Trajectory tracking experiment results:** In these tests, the module follows a vertical straight line and a circular path. We compare 3D target trajectories and actual module end-effector positions in (a) and (b). Furthermore, we provide RMS tracking errors with shaded error regions in cartesian coordinates in (c) and (d).

TABLE I

MODULE AND SENSOR DESIGN PARAMETERS

Module Parameters		**Sensor parameters**	
Angular RoM	40°	Linear RoM (Δx)	8 mm
Arm Width	30 mm	a	4 mm
Arm Length	50 mm	b	8.5 mm
Contracted Height	14 mm	c	3.4 mm
Extended Height	44 mm	d	3.3 mm
Total Mass	43 *g*		
Max. Linear Force	3 *N* *(@60 kPa)*		

Although it highly depends on the material and sealing utilized, our pouch motors can handle up to 150 kPa input pressure before bursting. Therefore, we supply a constant pneumatic pressure at 90 kPa to the control valves using a pressure gauge (SMC) to be on the safe side. We modulate the output pressure by driving the proportional valves with 12V PWM signals by converting 5V Arduino PWM signals to the 12V PWM signals using a transistor array. Moreover, we connect flyback diodes across the proportional valves to eliminate sudden voltage spikes and a capacitor between the ground and 12V to prevent fluctuations. The PID-based control algorithm running on the Arduino board creates the PWM signals. The controller receives the sensory feedback through wires. The overall experimental setup is shown in Figure 8.

To track a given trajectory, we calculate angular position setpoints for a given trajectory utilizing the proposed inverse kinematic model of the module. Moreover, we convert sensory voltage reading to actual leg angle positions. We give the errors between the angular setpoints and actual leg angles to the PID controller tuned by Ziegler–Nichols method. The controller computes the control PWM signal and drives the proportional valves. We record the measured angles to calculate the actual end-effector positions and compare them to the target trajectory.

To validate our models, embedded sensors, and pneumatic control method, we track two different trajectories: a vertical straight line with 10 mm length and a circular path with 3.6 *mm* diameter. We put a 50 *g* load on the module for the first trajectory and send a sinusoidal height reference input within the module's workspace. We conduct the second experiment with a 10 g load and send a circular reference input within the module's workspace. We repeat both experiments three times, record the target trajectory and the actual position of the end effector for two experiments, and, finally, compare them in Figure 9a and 9b in 3D. Moreover, in Figure 9c and 9d, we provide RMS tracking errors in cartesian axes with shaded error regions for both trajectories. The module successfully tracks the trajectories by reaching up to 1.5 mm/s end effector speed. Thus, this is the first time we report high fidelity controllability of not only this module but also other origami structures with embedded sensors using multiple pouch actuators as reliable means.

To evaluate the controller's tracking performance and bandwidth, we perform the vertical line tracking experiment by giving a sinusoidal reference input and doubling the frequency at each turn until we reach 10 Hz input. We repeat the experiment three times and calculate the RMS error for three cycles at each frequency and divide it by the maximum range of motion to normalize it. Figure 10 shows the results in a log-log plot.

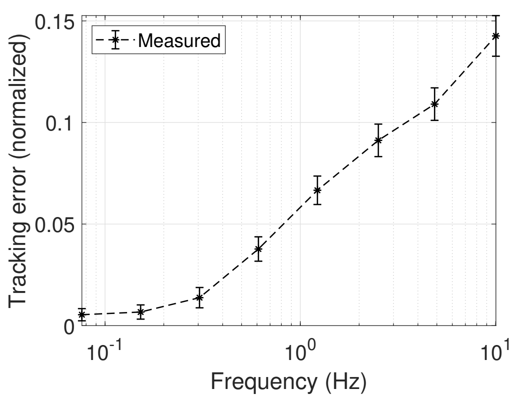

Fig. 10. **The results of the tracking of a sinusoidal reference input:** We conduct the trajectory tracking experiment by changing the frequency of the sinusoidal reference trajectory. We show RMS tracking error at different frequencies.

The tracking errors can be attributed to measurement errors, system delay, and controller performance. Especially, increasing the external load leads to larger errors and instability. We observe that the module can track the trajectories successfully with max load 50 g load. The performance can be improved by utilizing more complex control methods such as adaptive and discrete-time controls. Furthermore, after studying the dynamics of pouch motors and the module, model-based control techniques can be applied to improve the performance.

VI. Conclusion

This study presents models that allows the closed-loop position control of an origami-inspired module with a parallel kinematic chain utilizing soft pneumatic pouch actuators and a novel embedded sensor mechanism. The significance of this work lies in the possibility of having a completely *embedded system that is highly controllable despite the volume and non-linearity of the soft actuators.* Forward and inverse kinematic analysis of the module and sensor transmission enable us to track trajectories with precision. Novel embedded sensing method allows reliable and distributable angle sensing for origami mechanisms. Based on our closed-loop trajectory tracking results, we demonstrate that soft pouch actuators can be used for high fidelity position control of origami-inspired robots. Thus, the proposed module with embedded sensing and pneumatic actuation method allows the design of modular, safe, lightweight, scalable, reconfigurable, and controllable extra origami modules for wearable applications.

Acknowledgment

This work was supported the Swiss National Science Foundation (SNSF) and the National Centre of Competence in Research (NCCR) Robotics (Switzerland).

References

[1] Clark Davenport, Federico Parietti, and H Harry Asada. Design and biomechanical analysis of supernumerary robotic limbs. In *Dynamic Systems and Control Conference*, volume 45295, pages 787–793. American Society of Mechanical Engineers, 2012.

[2] Baldin Llorens-Bonilla, Federico Parietti, and H Harry Asada. Demonstration-based control of supernumerary robotic limbs. In *2012 IEEE/RSJ International Conference on Intelligent Robots and Systems*, pages 3936–3942. IEEE, 2012.

[3] Federico Parietti. *Design and control of supernumerary robotic limbs*. PhD thesis, Massachusetts Institute of Technology, 2016.

[4] Catherine Véronneau, Jeff Denis, Louis-Philippe Lebel, Marc Denninger, Vincent Blanchard, Alexandre Girard, and Jean-Sébastien Plante. Multifunctional remotely actuated 3-dof supernumerary robotic arm based on magnetorheological clutches and hydrostatic transmission lines. *IEEE Robotics and Automation Letters*, 5(2):2546–2553, 2020.

[5] Vighnesh Vatsal and Guy Hoffman. Wearing your arm on your sleeve: Studying usage contexts for a wearable robotic forearm. In *2017 26th IEEE International Symposium on Robot and Human Interactive Communication (RO-MAN)*, pages 974–980. IEEE, 2017.

[6] Vighnesh Vatsal and Guy Hoffman. Design and analysis of a wearable robotic forearm. In *2018 IEEE International Conference on Robotics and Automation (ICRA)*, pages 5489–5496. IEEE, 2018.

[7] Mohammed Al-Sada, Thomas Höglund, Mohamed Khamis, Jaryd Urbani, and Tatsuo Nakajima. Orochi: investigating requirements and expectations for multipurpose daily used supernumerary robotic limbs. In *Proceedings of the 10th Augmented Human International Conference 2019*, pages 1–9, 2019.

[8] Matthias Hofer and Raffaello D'Andrea. Design, fabrication, modeling and control of a fabric-based spherical robotic arm. *Mechatronics*, 68:102369, 2020.

[9] Srikanth Kolachalama and Sridhar Lakshmanan. Continuum robots for manipulation applications: A survey. *Journal of Robotics*, 2020, 2020.

[10] Hao Jiang, Zhanchi Wang, Yusong Jin, Xiaotong Chen, Peijin Li, Yinghao Gan, Sen Lin, and Xiaoping Chen. Design, control, and applications of a soft robotic arm. *arXiv preprint arXiv:2007.04047*, 2020.

[11] Hao Yang, Min Xu, Weihua Li, and Shiwu Zhang. Design and implementation of a soft robotic arm driven by sma coils. *IEEE Transactions on Industrial Electronics*, 66(8):6108–6116, 2018.

[12] Jasan Zughaibi, Matthias Hofer, and Raffaello D'Andrea. A fast and reliable pick-and-place application with a spherical soft robotic arm. *arXiv preprint arXiv:2011.04624*, 2020.

[13] Matteo Cianchetti, Maurizio Follador, Barbara Mazzolai, Paolo Dario, and Cecilia Laschi. Design and development of a soft robotic octopus arm exploiting embodied intelligence. In *2012 IEEE International Conference on Robotics and Automation*, pages 5271–5276. IEEE, 2012.

[14] Federico Renda, Michele Giorelli, Marcello Calisti, Matteo Cianchetti, and Cecilia Laschi. Dynamic model of a multibending soft robot arm driven by cables. *IEEE Transactions on Robotics*, 30(5):1109–1122, 2014.

[15] Ronghuai Qi, Amir Khajepour, William W Melek, Tin Lun Lam, and Yangsheng Xu. Design, kinematics, and control of a multijoint soft inflatable arm for human-safe interaction. *IEEE Transactions on Robotics*, 33(3):594–609, 2017.

[16] Shunichi Kurumaya, Hiroyuki Nabae, Gen Endo, and Koichi Suzumori. Exoskeleton inflatable robotic arm with thin mckibben muscle. In *2018 IEEE International Conference on Soft Robotics (RoboSoft)*, pages 120–125. IEEE, 2018.

[17] Xinquan Liang, Haris Cheong, Yi Sun, Jin Guo, Chee Kong Chui, and Chen-Hua Yeow. Design, characterization, and implementation of a two-dof fabric-based soft robotic arm. *IEEE Robotics and Automation Letters*, 3(3):2702–2709, 2018.

[18] Xinquan Liang, Haris Cheong, Chee Kong Chui, and Chen-Hua Yeow. A fabric-based wearable soft robotic limb. *Journal of Mechanisms and Robotics*, 11(3), 2019.

[19] Pham H Nguyen, IB Imran Mohd, Curtis Sparks, Francisco L Arellano, Wenlong Zhang, and Panagiotis Polygerinos. Fabric soft poly-limbs for physical assistance of daily living tasks. In *2019 International Conference on Robotics and Automation (ICRA)*, pages 8429–8435. IEEE, 2019.

[20] Pham Huy Nguyen, Curtis Sparks, Sai G Nuthi, Nicholas M Vale, and Panagiotis Polygerinos. Soft poly-limbs: Toward a new paradigm of mobile manipulation for daily living tasks. *Soft robotics*, 6(1):38–53, 2019.

[21] Matthew A Robertson and Jamie Paik. New soft robots really suck: Vacuum-powered systems empower diverse capabilities. *Science Robotics*, 2(9), 2017.

[22] Daniela Rus and Michael T Tolley. Design, fabrication and control of origami robots. *Nature Reviews Materials*, 3(6):101–112, 2018.

[23] Samuel Felton, Michael Tolley, Erik Demaine, Daniela Rus, and Robert Wood. A method for building self-folding machines. *Science*, 345(6197):644–646, 2014.

[24] Johannes TB Overvelde, Twan A De Jong, Yanina Shevchenko, Sergio A Becerra, George M Whitesides, James C Weaver, Chuck Hoberman, and Katia Bertoldi. A three-dimensional actuated origami-inspired transformable metamaterial with multiple degrees of freedom. *Nature communications*, 7(1):1–8, 2016.

[25] Cagdas D Onal, Michael T Tolley, Robert J Wood, and Daniela Rus. Origami-inspired printed robots. *IEEE/ASME transactions on mechatronics*, 20(5):2214–2221, 2014.

[26] Frederic H Giraud, Zhenishbek Zhakypov, and Jamie Paik. Design of low-profile compliant transmission mechanisms. In *2019 IEEE/RSJ International Conference on Intelligent Robots and Systems (IROS)*, pages 2700–2707. IEEE, 2019.

[27] Stefano Mintchev, Jun Shintake, and Dario Floreano. Bioinspired dual-stiffness origami. *Science Robotics*, 3(20), 2018.

[28] Zhenishbek Zhakypov, Florian Heremans, Aude Billard, and Jamie Paik. An origami-inspired reconfigurable suction gripper for picking objects with variable shape and size. *IEEE Robotics and Automation Letters*, 3(4):2894–2901, 2018.

[29] Zhenishbek Zhakypov, Kazuaki Mori, Koh Hosoda, and Jamie Paik. Designing minimal and scalable insect-inspired multi-locomotion millirobots. *Nature*, 571(7765):381–386, 2019.

[30] Dae-Young Lee, Sa-Reum Kim, Ji-Suk Kim, Jae-Jun Park, and Kyu-Jin Cho. Origami wheel transformer: A variable-diameter wheel drive robot using an origami structure. *Soft robotics*, 4(2):163–180, 2017.

[31] Suk-Jun Kim, Dae-Young Lee, Gwang-Pil Jung, and Kyu-Jin Cho. An origami-inspired, self-locking robotic arm that can be folded flat. *Science Robotics*, 3(16), 2018.

[32] Ketao Zhang, Chen Qiu, and Jian S Dai. An extensible continuum robot with integrated origami parallel modules. *Journal of Mechanisms and Robotics*, 8(3), 2016.

[33] J. Santoso, E. H. Skorina, M. Luo, R. Yan, and C. D. Onal. Design and analysis of an origami continuum manipulation module with torsional strength. In *2017 IEEE/RSJ International Conference on Intelligent Robots and Systems (IROS)*, pages 2098–2104, 2017.

[34] Junius Santoso and Cagdas D Onal. An origami continuum robot capable of precise motion through torsionally stiff body and smooth inverse kinematics. *Soft Robotics*, 2020.

[35] Christoph H Belke and Jamie Paik. Mori: a modular origami robot. *IEEE/ASME Transactions on Mechatronics*, 22(5):2153–2164, 2017.

[36] Noah T Jafferis, E Farrell Helbling, Michael Karpelson, and Robert J Wood. Untethered flight of an insect-sized flapping-wing microscale aerial vehicle. *Nature*, 570(7762):491–495, 2019.

[37] Amir Firouzeh and Jamie Paik. An under-actuated origami gripper with adjustable stiffness joints for multiple grasp modes. *Smart Materials and Structures*, 26(5):055035, 2017.

[38] M Salerno, F Zuliani, A Firouzeh, and J Paik. Design and control of a low profile electromagnetic actuator for foldable pop-up mechanisms. *Sensors and Actuators A: Physical*, 265:70–78, 2017.

[39] S Ahmed, Zoubeida Ounaies, and M Frecker. Investigating the performance and properties of dielectric elastomer actuators as a potential means to actuate origami structures. *Smart Materials and Structures*, 23(9):094003, 2014.

[40] Zhenishbek Zhakypov, Mustafa Mete, Julien Fiorentino, and Jamie Paik. Programmable fluidic networks design for robotic origami sequential self-folding. In *2019 2nd IEEE International Conference on Soft Robotics (RoboSoft)*, pages 814–820. IEEE, 2019.

[41] Shuguang Li, Daniel M Vogt, Daniela Rus, and Robert J Wood. Fluid-driven origami-inspired artificial muscles. *Proceedings of the National academy of Sciences*, 114(50):13132–13137, 2017.

[42] Panagiotis Polygerinos, Nikolaus Correll, Stephen A Morin, Bobak Mosadegh, Cagdas D Onal, Kirstin Petersen, Matteo Cianchetti, Michael T Tolley, and Robert F Shepherd. Soft robotics: Review of fluid-driven intrinsically soft devices; manufacturing, sensing, control, and applications in human-robot interaction. *Advanced Engineering Materials*, 19(12):1700016, 2017.

[43] Xu Sun, Samuel M Felton, Ryuma Niiyama, Robert J Wood, and Sangbae Kim. Self-folding and self-actuating robots: a pneumatic approach. In *2015 IEEE International Conference on Robotics and Automation (ICRA)*, pages 3160–3165. IEEE, 2015.

[44] Ryuma Niiyama, Xu Sun, Cynthia Sung, Byoungkwon An, Daniela Rus, and Sangbae Kim. Pouch motors: Printable soft actuators integrated with computational design. *Soft Robotics*, 2(2):59–70, 2015.

[45] I. Adibnazari, B. J. Jeon, Y. Park, and M. T. Tolley. Versatile rotary actuators for small-scale robotic systems. In *2020 3rd IEEE International Conference on Soft Robotics (RoboSoft)*, pages 873–878, 2020.

[46] Zhenishbek Zhakypov and Jamie Paik. Design methodology for constructing multimaterial origami robots and machines. *IEEE Transactions on Robotics*, 34(1):151–165, 2018.

[47] Xu Sun, Samuel M Felton, Robert J Wood, and Sangbae Kim. Printing angle sensors for foldable robots. In *2015 IEEE/RSJ International Conference on Intelligent Robots and Systems (IROS)*, pages 1725–1731. IEEE, 2015.

[48] Martin EW Nisser, Samuel M Felton, Michael T Tolley, Michael Rubenstein, and Robert J Wood. Feedback-controlled self-folding of autonomous robot collectives. In *2016 IEEE/RSJ International Conference on Intelligent Robots and Systems (IROS)*, pages 1254–1261. IEEE, 2016.

[49] Matthew A Robertson, Ozdemir Can Kara, and Jamie Paik. Soft pneumatic actuator-driven origami-inspired modular robotic “pneumagami”. *The International Journal of Robotics Research*, page 0278364920909905, 2020.

[50] Stephen L Canfield and Charles F Reinholtz. Development of the carpal robotic wrist. In *Experimental Robotics V*, pages 423–434. Springer, 1998.

[51] Marco Salerno, Ketao Zhang, Arianna Menciassi, and Jian S Dai. A novel 4-dof origami grasper with an sma-actuation system for minimally invasive surgery. *IEEE Transactions on Robotics*, 32(3):484–498, 2016.

[52] Marco Salerno, Jamie Paik, and Stefano Mintchev. Ori-pixel, a multi-dofs origami pixel for modular reconfigurable surfaces. *IEEE Robotics and Automation Letters*, 5(4):6988–6995, 2020.